

Multiple transitions between coherence resonances induced by mixed-mode bursting with complex fast-slow dynamics

Lirui Yuan(袁理睿), Huaguang Gu(古华光), and Juntian Li(李钧天)
Citation: Chin. Phys. B, 2026, 35 (**6**): 060506. DOI: 10.1088/1674-1056/ae5520
http://cpb.iphy.ac.cn; http://iopscience.iop.org/cpb

What follows is a list of articles you may be interested in

Complexity dynamics analysis of a dual-channel green supply chain with government intervention and cap-and-trade regulation

Yuhao Zhang(张玉豪), Lin Huang(黄林), and Man Yang(杨满)
Chin. Phys. B, 2025, 34 (**7**): 070501. DOI: 10.1088/1674-1056/adca9c

A novel non-autonomous hyperchaotic map based on discrete memristor parallel connection

Weiping Wu(吴伟平), Mengjiao Wang(王梦蛟), and Qigui Yang(杨启贵)
Chin. Phys. B, 2025, 34 (**5**): 050503. DOI: 10.1088/1674-1056/adb8bc

A novel variable-order fractional chaotic map and its dynamics

Zhouqing Tang(唐周青), Shaobo He(贺少波), Huihai Wang(王会海), Kehui Sun(孙克辉), Zhao Yao(姚昭), and Xianming Wu(吴先明)
Chin. Phys. B, 2024, 33 (**3**): 030503. DOI: 10.1088/1674-1056/ad1a93

Bifurcations for counterintuitive post-inhibitory rebound spike related to absence epilepsy and Parkinson disease

Xian-Jun Wang(王宪军), Hua-Guang Gu(古华光), Yan-Bing Jia(贾雁兵), Bo Lu(陆博), and Hui Zhou(周辉)
Chin. Phys. B, 2023, 32 (**9**): 090502. DOI: 10.1088/1674-1056/acd7d3

Prompt efficiency of energy harvesting by magnetic coupling of an improved bi-stable system

Hai-Tao Li(李海涛), Wei-Yang Qin(秦卫阳)
Chin. Phys. B, 2016, 25 (**11**): 110503. DOI: 10.1088/1674-1056/25/11/110503

SPECIAL TOPIC — Biophysical circuits: Modeling & applications in neuroscience

Multiple transitions between coherence resonances induced by mixed-mode bursting with complex fast–slow dynamics

Lirui Yuan(袁理睿), Huaguang Gu(古华光)[†], and Juntian Li(李钧天)

School of Aerospace Engineering and Applied Mechanics, Tongji University, Shanghai 201804, *China*

(Received 8 January 2026; revised manuscript received 18 March 2026; accepted manuscript online 20 March 2026)

Coherence resonance (CR) in neurons, which highlights the beneficial effects of noise, is generally induced from the resting state. In this study, multiple transitions between CR and anti-CR arise from mixed-mode bursting that includes a quiescent state (QS), bursting, and other dynamic behaviors. In addition to beginning from a saddle-node bifurcation and terminating at a limit-point bifurcation, the burst exhibits other special fast–slow dynamics, i.e., shuttling back and forth across the limit-point bifurcation twice to form two clusters of multiple spikes. These clusters are induced by cooperation among three factors: the coexistence of a stable focus and a limit cycle separated by an unstable limit cycle, the weak attraction of the stable focus due to the small negative real parts of its eigenvalues, and the dependence of the slow-variable nullcline on the membrane potential. Weak noise (D) can induce various numbers of clusters, resulting in various interburst intervals (IBIs) and burst durations (BDs). For strong D, the burst begins at a delayed phase and terminates at an advanced phase, resulting in the disappearance of the clusters and shortened IBIs and BDs. With increasing D, the number of clusters increases, decreases, increases, and then decreases, which induces similar changes in the coefficients of variation of the IBIs and BDs, i.e., multiple transitions between CR and anti-CR. The results include the special dynamics of a burst, a novel example of CR, the dynamic mechanism of CRs, and potential functions of synaptic noise in bursting neurons.

Keywords: coherence resonance, anti-coherence resonance, mixed-mode bursting, bifurcations

PACS: 05.45.–a, 87.19.lg

DOI: 10.1088/1674-1056/ae5520 **CSTR:** 32038.14.CPB.ae5520

1. Introduction

Coherence resonance (CR) and bursting are two important nonlinear phenomena that play various roles in the nervous system and are often studied independently.[1–3] CR shows that noise has a beneficial effect in modulating firing activities in single neurons and spatiotemporal patterns in networks,[4–6] for instance, enhancing information processing capacity.[7] As D increases, the coefficient of variation (CV) of interspike intervals (ISIs) decreases at first and then increases for CR, and the indicators of the power spectrum of firing trains manifest an inverse change.[1,2] CR generally appears around different bifurcations of equilibrium points induced by various noises.[8–10] This allows us to investigate different cases related to CR, such as anti-CR, multiple CRs, and spatial CR.[11,12] In contrast to CR, anti-CR shows that noise can inhibit firing and minimize coherence,[13–15] which generally arises from spiking near a bifurcation point or from the coexisting behaviors of the resting state and spiking.[16,17] For anti-CR, the CV of ISIs increases and then decreases.[18–20]

In addition to the spiking and resting states, bursting is another important electrical behavior of neurons,[21–23] which often exhibits a transition between two states: a quiescent state (QS) and continuous spiking.[5–7] Bursting also plays important roles in brain functions such as information processing, respiration,[24,25] and the regulation of blood pressure, as well as in brain diseases such as major depressive disorder,[26–28] Parkinson's disease,[29–31] seizures, and migraines.[32–34] In nonlinear dynamics, bursting is produced via the modulation of a slow variable on the fast subsystem.[5,7] In general, the fast subsystem can exhibit two types of bifurcations: from the resting state to the limit cycle and from the limit cycle to the equilibrium point.[35–37] Transitions between the two states of bursting often correspond to the two types of bifurcations.[38–40] Accordingly, different bursting patterns are named after the two types of bifurcations. For instance, the well-known 'fold/homoclinic' bursting[41] begins at a fold bifurcation and terminates at a homoclinic bifurcation.[42–44] In addition to the QS and continuous spiking,[45,46] a special bursting pattern called mixed-mode bursting often contains more dynamic behaviors, such as subthreshold oscillations or a depolarization block (DB).[47] Thus, mixed-mode bursting is associated with more bifurcations or more transitions between different behaviors, for instance, the bursting related to seizures and migraines. Various bursting patterns are observed in both biological experiments and theoretical models, but their underlying dynamic mechanisms remain unclear.[31,34] Moreover, it is well known that real neurons are influenced by various stochastic factors such as synaptic

[†]Corresponding author. E-mail: guhuaguang@tongji.edu.cn

© 2026 Chinese Physical Society and IOP Publishing Ltd. All rights, including for text and data mining, AI training, and similar technologies, are reserved.

noise and ionic channel noise.[48,49] Therefore, identifying the dynamics of bursting modulated by stochastic factors is very important. However, compared with studies of the effects of noise on the resting state and spiking, there are fewer studies on stochastic bursting.

Inspired by CR for the resting state and anti-CR for spiking, the phenomena of CR, anti-CR, and double CR have recently been extended to the study of bursting, and their dynamic mechanisms have been linked to the bifurcations underlying bursting, as revealed through fast–slow analysis.[50–52] For instance, anti-CR is induced by 'homoclinic/homoclinic' bursting, which is explained by the stochastic responses around the homoclinic bifurcation.[53] For 'fold/big homoclinic' bursting, CR is evoked and explained by stochastic dynamics around the big homoclinic bifurcation. Bursting that begins at a subcritical Hopf bifurcation (SubHB) and terminates at a limit point bifurcation of cycles (LPC), known as 'subHopf/LPC,' induces multiple CRs. These results show that bursting manifests complex stochastic dynamics and underlying fast–slow dynamics. Investigating these stochastic dynamics and their mechanisms remains a very important topic. Various bursting patterns have been reported in theoretical models and experiments,[1,31,34] but the stochastic dynamics of only a few bursting patterns have been studied.

In recent years, research into noise-induced resonance in neurons has advanced to the stage of brain network responses. Studies have found that resonance in brain networks suggests the existence of an optimal stimulation period when the brain is engaged in task states.[54] Furthermore, other studies have characterized neuronal resonance phenomena using success probability and introduced Gaussian colored noise to drive logical stochastic resonance.[55] A series of studies have further expanded the application of stochastic resonance in neuroscience.

In this paper, the stochastic dynamics and mechanisms of mixed-mode oscillation bursting with special fast–slow dynamics are investigated. Specifically, transitions from anti-CR to CR to anti-CR and to CR are observed, and the complex mechanism is elucidated. First, the mixed-mode characteristics, i.e., the QS, bursting, subthreshold oscillations, and the DB, are identified. Second, the complex fast–slow dynamics of the bursting are obtained, manifested as 'SNIC/LPC' bursting (where SNIC denotes a saddle-node bifurcation on an invariant cycle). In particular, in contrast to the general burst that terminates at an LPC,[50] the 'SNIC/LPC' burst shuttles back and forth across the LPC twice to form two clusters of spikes, induced by three factors. The first is that the stable focus coexists with stable limit cycles (SLCs), which are separated by an unstable limit cycle (ULC). The second factor is that the stable focus has a small negative real part of its eigenvalue, which results in a relatively weak attraction capacity. The last factor is the nullcline of the slow variable, which induces an increase in the slow variable at low membrane potentials. The complex dynamics of the two clusters around the LPC are novel characteristics of the bursting. Finally, the stochastic dynamics of bursting and its dynamic mechanism are obtained. Weak noise mainly induces different numbers of clusters, resulting in various interburst intervals (IBIs) and burst durations (BDs). In the presence of strong noise, the burst begins at a delayed phase and terminates at an advanced phase, which causes the IBIs and BDs to shorten. With increasing noise intensity, the number of clusters and the CVs of the IBIs and BDs increase, decrease, increase, and then decrease, showing multiple transitions between CR and anti-CR. Furthermore, the results of spectral analysis reveal that the stochastic system undergoes an identical resonant transition. The results not only present a novel candidate for investigating CRs in bursting with novel fast–slow dynamics but also provide insights into the potential effects of synaptic noise on bursting.

The rest of this paper consists of Sections 2, 3, and 4, which respectively present the models and methods, results, and conclusions.

2. Models and methods

2.1. Deterministic and stochastic Morris–Lecar–Terman models

A dimensionless Morris–Lecar–Terman (MLT) model proposed in Ref. [56] for describing bursting activity is as follows:

$$C\frac{\mathrm{d}V}{\mathrm{d}t} = I_{\mathrm{K}} + I_{\mathrm{Ca}} + I_{\mathrm{L}} + y + I_{\mathrm{app}}, \tag{1}$$

$$\frac{\mathrm{d}\omega}{\mathrm{d}t} = \frac{\omega_{\infty} - \omega}{\tau_{\omega}}, \tag{2}$$

$$\frac{\mathrm{d}y}{\mathrm{d}t} = r(k - V), \tag{3}$$

where the variables V, ω, and y denote the membrane potential, the activation of the potassium ion channel, and the inactivation of ion channels, respectively. C is the membrane capacitance. I_{app} refers to the externally injected current. $I_{\mathrm{K}} = -g_{\mathrm{K}}\omega(V - E_{\mathrm{K}})$, $I_{\mathrm{Ca}} = -g_{\mathrm{Ca}}m_{\infty}(V - E_{\mathrm{Ca}})$, and $I_{\mathrm{L}} = -g_{\mathrm{L}}(V - E_{\mathrm{L}})$ respectively represent the potassium, calcium, and leakage currents. The corresponding conductances are labeled g_{K}, g_{Ca}, and g_{L}, and the reversal potentials are E_{K}, E_{Ca}, and E_{L}. $\omega_{\infty} = \frac{1}{2}[1 + \tanh(\frac{V - c_3}{c_4})]$ and $m_{\infty} = \frac{1}{2}[1 + \tanh(\frac{V - c_1}{c_2})]$ denote the steady-state activation of the potassium and calcium channels, and $\tau_{\omega} = \left[\cosh(\frac{V - c_3}{2c_4})/\tau_0\right]^{-1}$ is the time constant. The threshold voltage for calcium channel activation is denoted by c_1, the slope parameter of the activation curve is c_2, the threshold voltage for potassium channel activation is denoted by c_3, and the slope parameter of the potassium channel activation curve is c_4. In the time constant expressions, the

subscript ∞ denotes 'steady state', i.e., the equilibrium open probability of the ion channel when the voltage is held constant. Finally, τ_0 is the baseline timescale parameter for potassium channel kinetics. r is the timescale separation coefficient, and k is considered a key bifurcation parameter of the system. The parameter values are listed in Table 1.

Table 1. Parameters of the MLT model.

Parameter	Value	Parameter	Value	Parameter	Value
C	1.0	E_{Ca}	1.0	c_4	0.16
g_K	2.0	E_L	−0.5	τ_0	3.0
g_{Ca}	1.25	c_1	−0.01	r	0.003
g_L	0.5	c_2	0.15	k	−0.038
E_K	−0.7	c_3	0.1	I_{app}	0

In fact, the MLT model is derived from the Morris–Lecar (ML) model by introducing the inactivation of ion channels, represented by y. Its dimensionless process is similar to that of the ML model.[57] The original ML model without the dimensionless process exhibits spiking with frequencies within physiological ranges. The improved MLT model with the dimensionless process can yield bursting patterns related to physiological functions,[56] offering greater biological plausibility. Therefore, in the spectral analysis of the MLT model conducted in this study, the time dimension retains the unit of milliseconds (ms) from the original ML model before dimensionless processing was introduced. This approach does not affect the dynamical analysis of the system with respect to the variable y.

Stochastic dynamics are considered in this paper, so a Gaussian white noise $\xi(t)$ is introduced into Eq. (1) while Eqs. (2) and (3) remain unchanged, thus forming the stochastic MLT model. The first equation is as follows:

$$C\frac{\mathrm{d}V}{\mathrm{d}t} = I_K + I_{Ca} + I_L + y + \xi(t). \tag{4}$$

The characteristics of $\xi(t)$ are as follows: $\langle\xi(t)\rangle = 0$ and $\langle\xi(t)\xi(t')\rangle = 2D\delta(t-t')$, where D is the noise intensity, $\langle\cdot\rangle$ is the average, and $\delta(\cdot)$ is the Dirac δ function.

2.2. Metric used to characterize CR

The method used to characterize CR through changes in the CV, as proposed in Ref. [1], is also used in this paper. For an indicator X, the CV measures the ratio of the standard deviation (SD) to the mean, which is expressed as follows:

$$\mathrm{CV} = \frac{\sqrt{\frac{1}{N-1}\sum_{i=1}^{N}\left(X_i - \frac{1}{N}\sum_{i=1}^{N}X_i\right)^2}}{\frac{1}{N}\sum_{i=1}^{N}X_i}. \tag{5}$$

Here, X represents either BDs or IBIs. The CV first decreases and then increases with increasing D, which denotes the occurrence of CR. If the CV manifests an inverse change, this indicates the occurrence of anti-CR.

In addition, the power spectrum of bursting trains has been widely used to characterize CR.[51] The power spectrum of V in the MLT model was obtained using the fast Fourier transform (FFT). If the peak value of the power spectrum first increases and then decreases with increasing D, CR is produced. If the peak value of the power spectrum first decreases and then increases with increasing D, anti-CR is produced. To perform spectral analysis on the V data, the time unit used for data sampling in this paper is set to milliseconds, which is consistent with the time unit in the original ML model.

2.3. Fast–slow analysis to the bursting and y-nullcline

Fast–slow variable dissection has been widely used to identify the dynamics of bursting.[5,7,20] This method is grounded in the significant timescale separation between the state variables in neuronal systems, leading to a partitioning into a fast subsystem and slow variables. The fast subsystem governs the rapid generation of individual action potentials, while the slow variables gradually modulate the initiation and termination phases of action potentials. By treating the slow variables as quasi-static parameters and obtaining the equilibrium states and bifurcations of the fast subsystem, the switching mechanisms between spikes and QSs during bursting can be elucidated.

Notably, the parameter $r = 0.003$ in Eq. (3) represents the timescale separation coefficient of y relative to V. According to singular perturbation theory, the presence of r makes the variable y three orders of magnitude smaller than V, so y can be regarded as the slow variable of the system.[57] Consequently, the fast subsystem consists of Eqs. (1) and (2). The nullcline of the slow variable y is $\mathrm{d}y/\mathrm{d}t = r(k-V) = 0$, i.e., $V = k$. The more negative V is (i.e., lower than k), the more positive $\mathrm{d}y/\mathrm{d}t$ is. The more positive V is (i.e., higher than k), the more negative $\mathrm{d}y/\mathrm{d}t$ is. In this paper, by defining the variable y as the bifurcation parameter, the dynamics of V with respect to y can be precisely obtained, as shown in Fig. 3(a). By superimposing the phase trajectory of mixed-mode bursting onto the bifurcation diagram, the underlying dynamics of bursting generation can be elucidated.

2.4. Method

In this paper, fourth-order Runge–Kutta integration is used to solve the equations, and the time step assigned is 0.001. Bifurcation analysis is performed using the AUTO package in XPPAUT.[58]

3. Results

3.1. Dynamics of deterministic bursting

3.1.1. The mixed-mode characteristics of the bursting

The two-parameter bifurcation diagram of the system with respect to the parameters k and I_{app} is shown in Fig. 1.

It is worth noting that the dynamics of the system with respect to the parameter k are independent of the magnitude of the parameter $I_{\rm app}$. In the two-parameter bifurcation diagram, this causes the bifurcation curves for torus bifurcation (TR) and Hopf bifurcation (HB) to appear as two vertical lines. The relevant mathematical proof is provided in Appendix A.

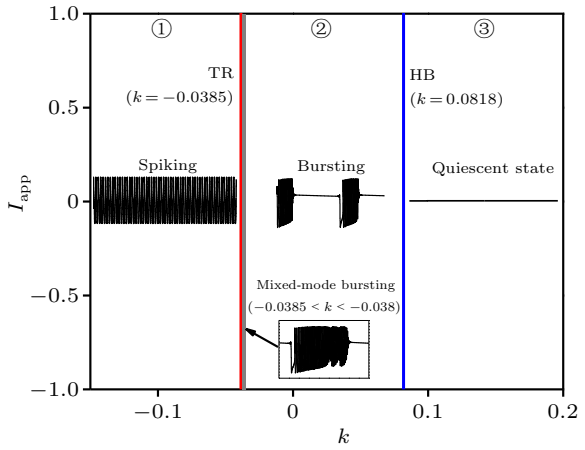


Fig. 1. Bifurcation in the plane (k, $I_{\rm app}$) of the system. Regions ①, ②, and ③ represent the system's spiking region, bursting region, and QS region, respectively.

As shown in Fig. 1, the two-parameter bifurcation plane is divided by TR and HB into three regions, ①, ②, and ③, corresponding to tonic spiking, bursting, and the QS of the system, respectively. Simulations reveal that within the gray parameter region to the right of the TR curve ($-0.0385 < k < -0.038$), the system exhibits a complex mixed-mode bursting state. Based on this mixed-mode bursting, this paper investigates the dynamics of noise-induced multiple resonance transitions in the system.

A mixed-mode burst is simulated for $k = -0.038$ and $I_{\rm app} = 0$, as illustrated in Fig. 2(a), with a period illustrated in Fig.2(b). The period begins at point B' and terminates at point B, with a spike defined as occurring when the membrane potential V exceeds 0.25 (red dashed line). Within one period, we observe a short QS, a very long BD, a damping subthreshold oscillation (SO1), a segment of DB, and a growing subthreshold oscillation (SO2). SO1 terminates at point C, and SO2 begins at point A. The IBI for the bursting is ~ 821, as illustrated in Fig. 2(b). Within the burst, the ISIs range from 8.9 to 18.3.

3.1.2. Three phases of the slow variable y

As depicted in Fig. 2(c), the slow variable y contains three phases within one period, which are discussed below.

(i) A slow increase (left black) in y, with oscillations, which corresponds to the QS and the former part of the burst with increasing minimal V ($V_{\rm min}$), is labeled as phase '0'. The y-nullcline $V = k = -0.038$, i.e., $V = -0.038$, is illustrated by a dashed orange line in Fig. 2(b). Then, y decreases ($\mathrm{d}y/\mathrm{d}t < 0$) for $V < -0.038$, and y increases ($\mathrm{d}y/\mathrm{d}t > 0$) for $V < -0.038$. If $V_{\rm min}$ increases spike by spike, the maximal value of $\mathrm{d}y/\mathrm{d}t$, which appears around $V_{\rm min}$, becomes smaller, resulting in a small increase of y spike by spike.

(ii) Small oscillations around a high level of y (blue and magenta) correspond to the second part of the burst. Two clusters of spikes (blue and magenta) appear, with the blue and magenta clusters labeled as 'I' and 'II', respectively. For both clusters, $V_{\rm min}$ first becomes more negative and then less negative. The dynamics of the two clusters are very important and novel, and thus the bursting is classified as '2' in this paper, as addressed in Subsection 3.2.3.

(iii) The phases SO1, DB, and SO2 are characterized by a monostable decrease in y.

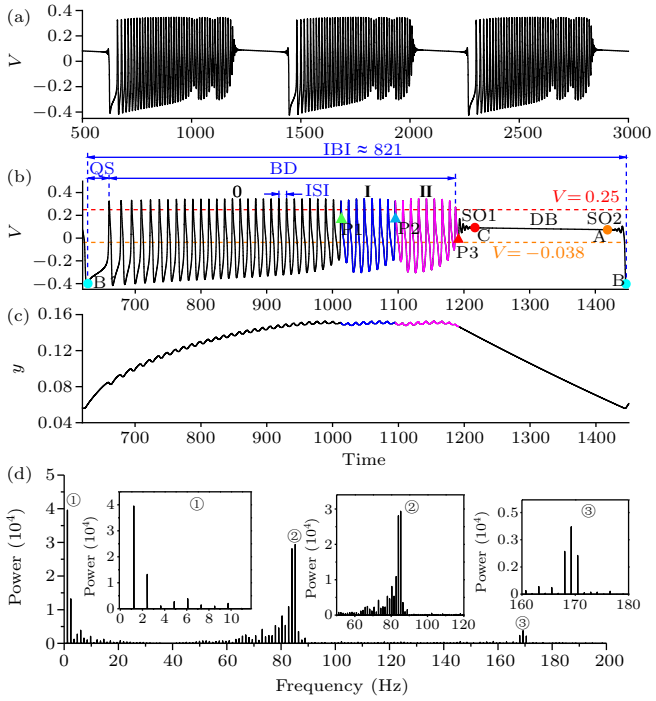


Fig. 2. Mixed-mode bursting for $k = -0.038$, $I_{\rm app} = 0$. (a) Membrane potential V. (b) A period of the bursting, containing two clusters of spikes (blue and magenta). (c) Three phases of the slow variable y. (d) Power spectrum. Peaks ①, ②, and ③ correspond to ~ 1.22 Hz, ~ 85.2 Hz, and ~ 169.2 Hz, respectively.

3.1.3. Power spectra of bursting activity and its different phases

The IBI for the burst is ~ 821, as shown in Fig. 2(b), corresponding to 1.22 Hz. The ISIs within the burst vary from 8.9 to 18.3, with an ISI approximating 12 labeled. The frequency of spontaneous ISIs is between 54.6 Hz and 112.4 Hz. The intervals between spikes of SO1 and SO2 are about 5.9, corresponding to 169.5 Hz. These frequencies can be found in the spectrum of the burst, as shown in Fig. 2(d).

The power spectrum of the deterministic bursting exhibits three dominant peaks, as presented in Fig. 2(d). The first dominant peak is labeled ①, with a frequency of around 1.2 Hz, corresponding to the IBIs. The peak height is approximately 4.0×10^4. The second peak is labeled ②, appearing at around

85.2 Hz and corresponding to the ISIs. The last peak, labeled ③, is located approximately at 169.2 Hz and corresponds to SO1 and SO2. After the introduction of noise, the dynamical behavior corresponding to peak effectively characterizes the noise-induced stochastic resonance transition of the system. The specific investigation is detailed in Subsection 3.5.

3.2. Fast–slow dynamics of the deterministic bursting

3.2.1. Fast subsystem: bifurcations and eigenvalue of the focus on the top branch

For the fast subsystem, bifurcations are depicted in Fig. 3(a) for increasing values of y. The equilibrium points exhibit an inverted Z-shaped curve, ignoring the left part of the middle and top branches (black dashed curves). The lower-left and upper-right red curves denote the stable node and the focus, respectively. As y increases, the stable node disappears via an SNIC, and an SLC (green) occurs. On the top branch, the unstable focus (upper black dashed curve) changes to a stable focus (upper-right red line) via a subHB, from which a ULC (dashed blue) emerges. The SLC and ULC collide and form an LPC. Near the LPC, the SLC (green) and stable focus (right red) coexist, which are separated by the ULC. The complex dynamics around the LPC can be used to explain the dynamics of two clusters (Figs. 6 and 7). In particular, the minimal V of the SLC (lower green) increases, which explains the elevated $V_{\min}$ of spikes in phase '0' (Fig. 4(c)).

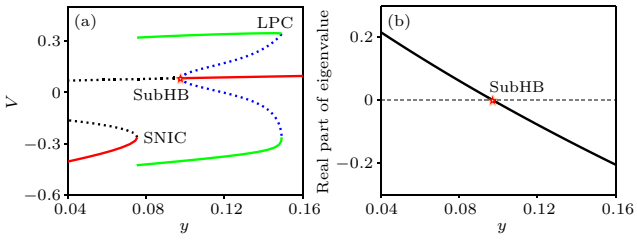


Fig. 3. Dynamics of the fast subsystem: (a) bifurcations; (b) real part of the eigenvalue of focus on the top branch.

For the unstable and stable foci separated by the subHB on the top branch, the real part of the eigenvalue is depicted in Fig. 3(b). The negative and positive real parts are located on the left and right of the subHB, respectively. As y moves away from the subHB, although the magnitude of the real part becomes large, its absolute value is relatively small. The small absolute values induce two characteristics, described as follows.

(i) The attractive capacity of the stable focus to the right of the subHB is weak, since its negative real part is small. If the trajectory to the right of the subHB is far from the stable focus in terms of V, the trajectory approaches the stable focus slowly and the amplitude decreases slowly, which can be used to explain the complex dynamics of the two clusters ('I' and 'II') and SO1 (Fig. 6).

(ii) The repulsive capacity of the unstable focus to the left of the subHB is weak because the real part of its eigenvalue is small and positive. If the trajectory to the left of the subHB is near the unstable focus in V, the trajectory leaves the unstable focus slowly, which can be used to detect the dynamics of DB and SO2. The DB to the left of the subHB can run along the unstable focus, and SO2 leaves the unstable focus slowly (Fig. 4(b)).

3.2.2. Burst terminates around the LPC and begins from an SNIC

By superimposing the (y, V) trajectories of different segments of bursting onto the bifurcation diagram in Fig. 3(a), the fast–slow dynamics of bursting is obtained, as shown in Fig. 4. The behavior of phase '0' (left black in Fig. 2(b)) begins at point B', as illustrated in Fig. 4(a). Before crossing the SNIC, the behavior corresponds to a short QS. Following the SNIC, the spikes move along the SLC (green) and proceed toward the LPC, forming the burst. As the number of spikes increases, $V_{\min}$ rises due to the increase in the minimal V (lower green) of the SLC. The dashed orange line corresponds to the y-nullcline, $V = -0.038$. Regions above and below the y-nullcline represent a decrease and an increase in y, respectively. It can be speculated that if strong noise were introduced, the burst would terminate at a phase to the left of the LPC, resulting in shortened BDs and IBIs.

The trajectories of SO1, DB, and SO2 are shown in Fig. 4(b), running from right to left. These trajectories are located to the left of the LPC. The beginning of SO1 corresponds to the termination of the burst, and the burst terminates around the LPC.

3.2.3. Depolarization block runs along the focus on the top branch

As depicted in Fig. 4(b), the SO1 following the burst shrinks to the stable focus (upper-right red line) and then runs along the stable focus (red line to the right) from right to left (i.e., with decreasing y), forming the DB. After running across the subHB, the DB continues to run along the unstable focus, since the real part of the eigenvalue has a very small positive value (Fig. 3(b)). At a location to the left of the SNIC, the amplitude of subthreshold oscillations grows, since the real part of the eigenvalue increases (Fig. 3(b)), and there is attraction from the stable node (left red) on the bottom branch, forming SO2. Finally, the plotted value drops to the neighborhood of the stable node (lower-left red line), resulting in the period terminating at point B. In the phase space, point B overlaps with point B'. It can be speculated that if strong noise were introduced, the DB would terminate earlier (i.e., further to the right), leading to a shortened IBI. If the termination phase were to the right of the SNIC and the burst began from a phase later than the SNIC, the result would be a shortening of the IBI and the BD.

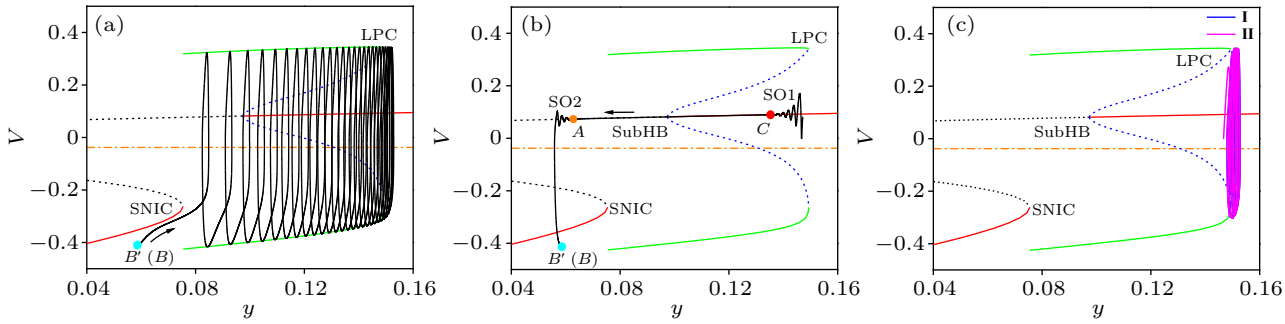


Fig. 4. Fast–slow dynamics for three phases of bursting: (a) phase '0'; (b) SO1, DB, and SO2; (c) clusters 'I' and 'II'.

3.2.4. Two clusters that are novel behaviors are due to the small negative real part of the eigenvalue

As the two clusters are plotted with the same size as those in Figs. 4(a) and 4(b), the two clusters show a very narrow range in y around the LPC, as shown in Fig. 4(c). The two clusters lie between the burst for phase '0' and SO1, which is a novel result that differs from the previously studied bursting that terminates at the LPC.[50] In the previous study, after running across the LPC, the burst changed directly to subthreshold oscillations, i.e. without clusters. In fact, these two clusters are induced by the cooperation of nonlinear dynamics for three reasons: one is the weak attraction of the stable focus induced by the small negative real part (Fig. 3(b)). If the real part were more negative, the behavior would be attracted to the stable focus more strongly, forming subthreshold oscillations that would directly terminate the burst. Consequently, clusters would not form. The cooperation between the three factors that leads to the appearance of the two clusters is addressed in detail in the following subsection, with the dynamics plotted on an expanded scale in the y-direction (Figs. 5–7).

3.3. Cooperation between three factors leading to the appearance of two clusters

3.3.1. Complex dynamic process and fast–slow dynamics of the two clusters

The V and y values for clusters 'I' (blue) and 'II' (magenta) are illustrated in Figs. 5(a1) and 5(a2), respectively, with $V_{\min}$ and maximal V ($V_{\max}$) labeled with stars and circles, respectively. The sequential numbers are also labeled. There are seven spikes for cluster 'I' and eight spikes for cluster 'II.' The first $V_{\min}$ for cluster 'I' is lower than the final $V_{\min}$ in phase '0', and the first $V_{\min}$ for cluster 'II' is lower than the last $V_{\min}$ for cluster 'I'. For both clusters, the $V_{\min}$ values for different spikes exhibit large variations; however, $V_{\max}$ manifests small variations. This distinction is important, since $V_{\min}$ determines the increase in y, while $V_{\max}$ determines the decrease in y. For both clusters, from spike 1 to spike 2, the value of y decreases. From spike 3 to spike 5, the level of y increases. For the last few spikes, the level of y decreases. In particular, the y values of points P1, P1′, and P2 equal those of the LPC.

The fast–slow dynamics of cluster 'I' (blue) and cluster 'II' (magenta) are shown individually in Figs. 5(b1) and 5(b2), respectively. Their combined dynamics are plotted accordingly in Fig. 5(b3), which presents a structure too complex for easy interpretation. To elucidate the detailed dynamics of the two clusters, the results for individual spikes are presented in Figs. 6 and 7.

3.3.2. Cooperation between three factors for cluster 'I'

The results for cluster 'I' are addressed in detail in Fig. 6. Cluster 'I' is induced by the cooperation of the following three factors.

The first factor is related to the weak attraction capacity of the stable focus, determined by the small real part of the eigenvalue. The behavior to the right of the LPC or within the ULC exhibits a slowly shrinking amplitude with increasing time, mainly due to the increase in $V_{\min}$. However, $V_{\max}$ remains nearly unchanged, since there is a small derivative over a wide range of $V_{\min}$ but a large derivative near the peak $V_{\max}$. For instance, spike 1 following point '0' (the end of phase '0') and spike 2 are shown in Fig. 6(a). The $V_{\min}$ of spike 1 increases, as it is attracted by the stable focus. Although the behavior following point P1 (whose y value equals that of the LPC) is to the left of the LPC, it is still within the ULC. Its $V_{\min}$ remains far from the stable focus, since the attraction is weak. Spike 2 is an exception, as part of it lies outside the ULC (dashed blue); this is addressed in factor 3. Spikes 3, 4, and 5 are shown in Fig. 6(b). Spikes 4 and 5 exhibit elevated values of $V_{\min}$, since they are to the right of the LPC or within the ULC. Spike 3 resembles spike 2. Spikes 6 and 7 are shown in Fig. 6(c), exhibiting elevated $V_{\min}$, since they are to the right of the LPC. However, from spike 3 to spike 7, the degree of increase in $V_{\min}$ is relatively small, since the $V_{\min}$ of spike 7 remains far from the stable focus.

The second factor is related to the y-nullcline, which depends on V. The value of y increases when V is below the y-nullcline and decreases when V is above it. For a spike, a more negative $V_{\min}$ induces a larger increase in the level of y, and a more positive $V_{\max}$ induces a smaller decrease in the level of y. The difference in $V_{\max}$ between different spikes is small; however, the difference in $V_{\min}$ is large. Therefore, spikes with more negative $V_{\min}$, such as spikes 2, 3, 4, and

5, move to the right, increasing the value of y. Spikes with less negative $V_{\min}$, such as spikes 1, 6, and 7, move to the left, decreasing the value of y.

The last factor is related to the coexistence of the stable focus and the SLC, which are separated by the ULC. This factor explains the reduced $V_{\min}$ of spikes 2 and 3. Following phase '0', spike 1 is close to the LPC, as shown in Fig. 6(a). Spike 1 mainly moves to the left (due to factor 2), and part of it lies to the left of the LPC after point P1. However, its amplitude is not small (due to factor 1). Therefore, the trajectory does not shrink to the stable focus to terminate the burst. Following the $V_{\max}$ of spike 1, the y-value for spike 2 first decreases, placing the trajectory to the left of the LPC. After crossing the y-nullcline, y increases, causing the trajectory to cross the ULC (lower dashed blue) and move outside it. Consequently, the trajectory moves along the SLC (green), resulting in a reduced $V_{\min}$. After crossing point P1′ (where y equals the y-value of the LPC) from left to right, the trajectory continues to the right of the LPC. For spike 3 (which follows spike 2), the behavior is similar, as shown in Fig. 6(b).

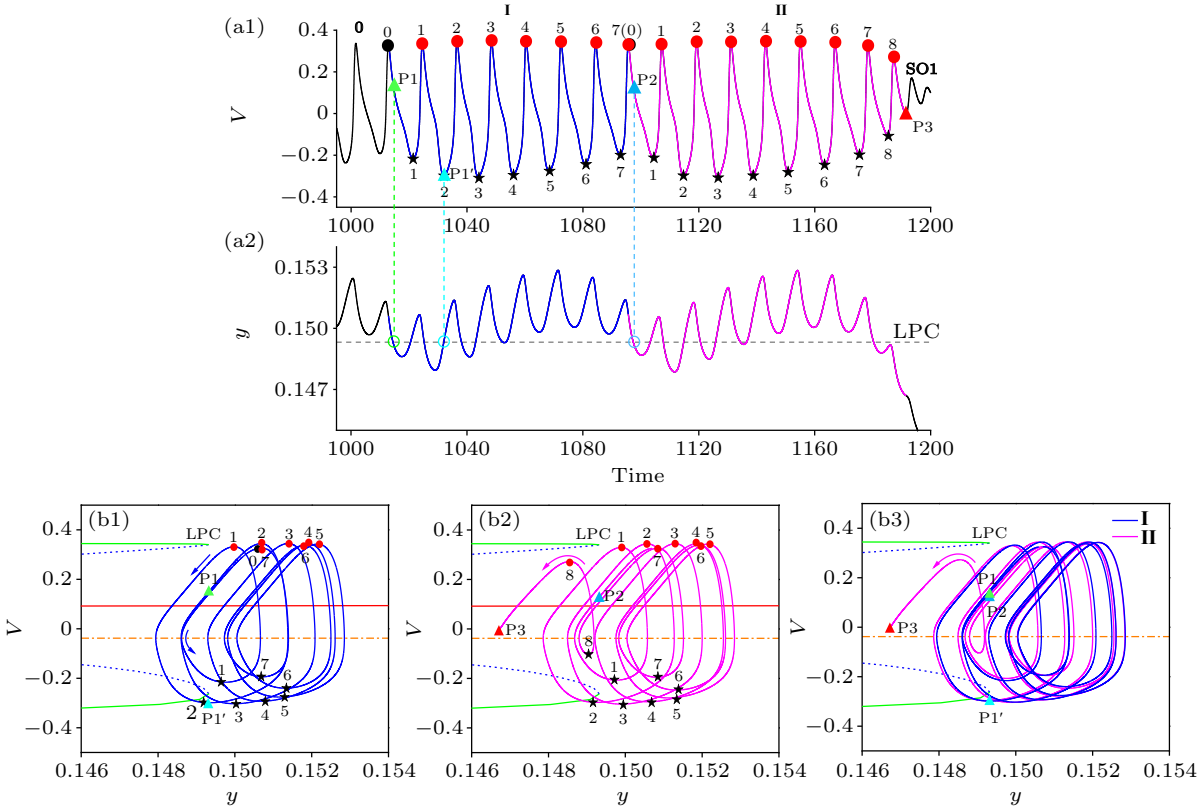


Fig. 5. Dynamics of clusters 'I' (blue) and 'II' (magenta). Time series: (a1) V; (a2) y. Fast–slow dynamics: (b1) cluster 'I'; (b2) cluster 'II'; (b3) clusters 'I' (blue) and 'II' (magenta). P3 is the termination phase of cluster 'II,' corresponding to $V_{\min}$.

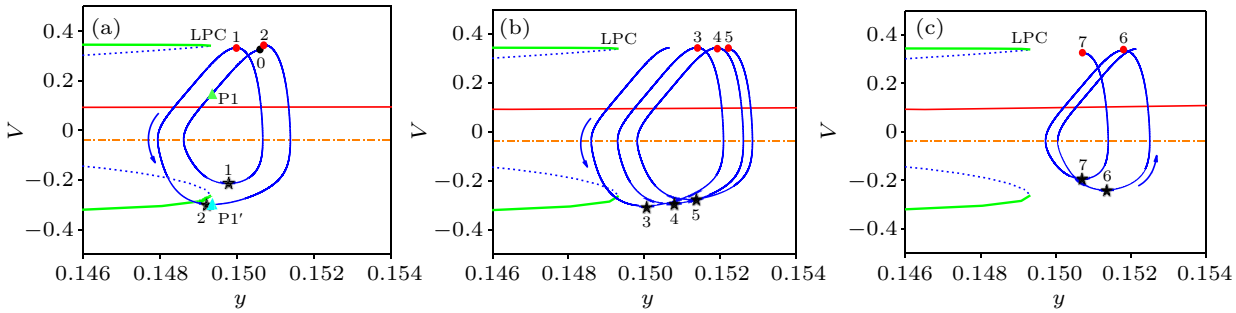


Fig. 6. Fast–slow dynamics of cluster 'I': (a) spikes 1 and 2; (b) spikes 3, 4, and 5; (c) spikes 6 and 7.

3.3.3. Cluster 'II' resembles cluster 'I', except for the termination of the burst (spike 8)

Next, the results for different spikes of cluster 'II' are depicted in the upper row of Fig. 7, and the results for clusters 'I' and 'II' are shown in the lower row. Spikes 1 and 2 of cluster 'II' are shown in Fig. 7(a1); they exhibit dynamics similar to those of cluster 'I' (Fig. 6(a)), and this similarity is depicted in Fig. 7(a2). Spikes 3, 4, and 5 of cluster 'II' are shown in Fig. 7(b1). Their dynamics resemble those of cluster 'I' (Fig. 6(b)), as illustrated in Fig. 7(b2). Spikes 6, 7, and 8 of cluster 'II' are shown in Fig. 7(c1). The dynamics of spikes 6 and 7 are similar to those of cluster 'I' (Fig. 6(c)), as illustrated

in Fig. 7(c2).

However, spike 6 of cluster 'II' is located slightly to the right of its counterpart in cluster 'I', and spike 7 of cluster 'II' is also located slightly to the right of its counterpart in cluster 'I'. Therefore, cluster 'II' manifests an essential distinction from cluster 'I'. Following spike 7 of cluster 'II', the trajectory cannot move outside the ULC, resulting in spike 8, which moves to the left. Spike 8 is located to the left of the LPC and inside the ULC and exhibits a damped V amplitude, as depicted in Figs. 7(c1) and 7(c2). Consequently, following spike 8 (point P3), SO2 appears instead of another cluster; that is, the two clusters terminate. The reduced amplitude of spike 7 in cluster 'II', along with the appearance of spike 8 within the ULC and to the left of the LPC, causes the burst to terminate.

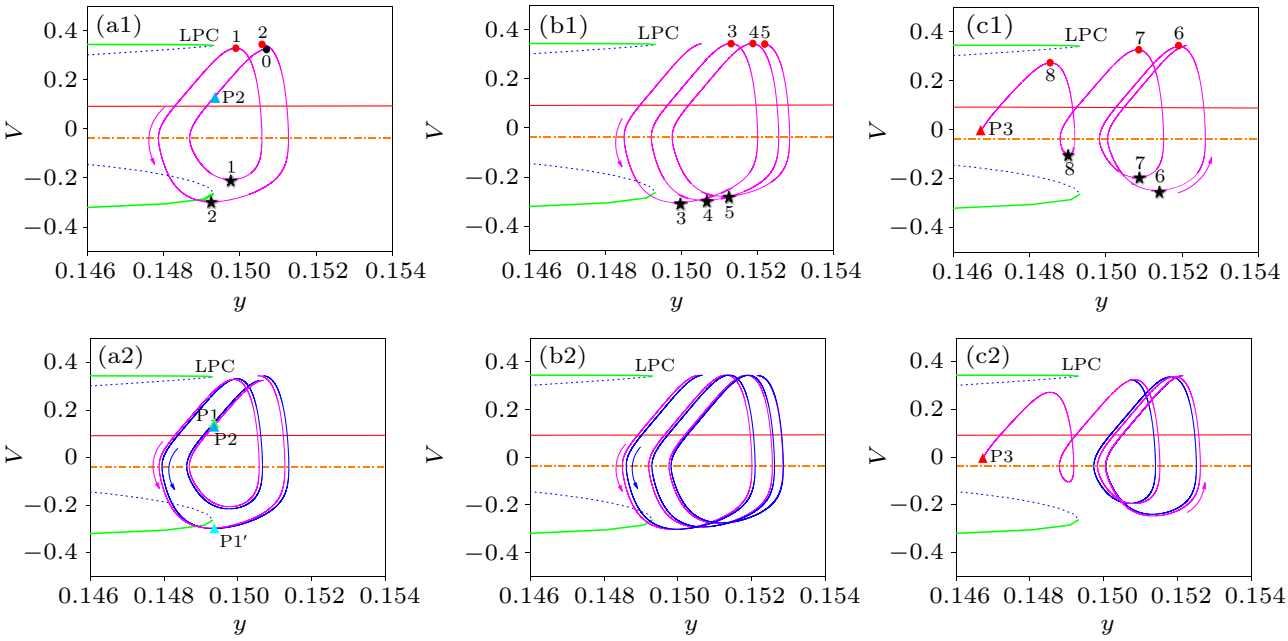


Fig. 7. Fast–slow dynamics of cluster 'II' (upper row) and clusters 'I' (blue) and 'II' (magenta) (lower row). (a1) and (a2) Spikes 1 and 2; (b1) and (b2) spikes 3, 4, and 5. (c1) and (c2) The last few spikes.

3.3.4. Speculation on stochastic bursts with n clusters at weak noise intensity

The complex dynamics of clusters 'I' and 'II' can be used to explain the stochastic dynamics around the LPC, i.e., the formation of stochastic clusters. Since spike 8 is close to the ULC (Figs. 7(c1) and 7(c2)), suitable (i.e., not overly strong) noise can induce the behavior near its location to cross the ULC, forming another cluster. Thus, in the stochastic model, bursts whose cluster count is equal to or different from two can be evoked. For convenience, a burst with n clusters is labeled n. Notably, a burst n with $n > 2$ results in prolonged IBI and BD, as opposed to the case of strong noise, which can shorten the IBI and the BD, as speculated in Subsection 3.2.2.

3.4. Stochastic bursting patterns and transitions between CR and anti-CR

3.4.1. Bursts at weak D: trains of bursting with different numbers of clusters

Ten representative stochastic bursts with different cluster counts are presented across ten rows in Fig. 8. In each row, the left, middle, and right columns correspond to V, y, and the fast–slow dynamics, respectively. The corresponding noise intensity D is indicated in each panel.

In the stochastic system, if an ISI exceeds 20, a QS or a DB appears. Then, a burst containing multiple spikes appears between two ISIs greater than 20. Within a burst, the local minimal values of $V(t)$ (V_{mini}, stars in Fig. 5(a1)) are obtained, and a cluster appears between two consecutive maximal values of V_{mini}. If V_{mini} increases monotonically, only the bursts '0', '0-', or '0- -' appear, i.e., without clustering, as illustrated by the black phase in the left-hand column of Fig. 8.

The first seven representatives with colorful subsegments correspond to weak noise. Following phase '0' (black), different clusters are labeled with different colors. The numbers of clusters are 7, 6, 5, 4, 3, 2, and 1, respectively. Accordingly, these bursts are labeled as '7,' '6,' '5,' '4,' '3,' '2,' and '1' in this paper. At a fixed level of D, such as 1×10^{-8}, bursts with different clusters can appear, such as '6' in Fig. 8(a2) and '5' in Fig. 8(a3). For bursts at the same D, a larger cluster number correlates with a longer BD. Bursts '4,' '3,' '2,' and '1' at $D = 1 \times 10^{-6}$ show similar dynamics. At $D = 1 \times 10^{-3}$, burst '7' appears. Its duration is shorter than that of burst '6' at $D = 1 \times 10^{-8}$, suggesting that higher noise levels can lead to shorter burst durations. Similarly, in the eighth example (Fig. 8(a8)), burst '0' without clusters appears at $D = 1 \times 10^{-4}$, which is relatively short. The burst exhibits only a basic subsegment '0' (Fig. 2(b)), with no clusters.

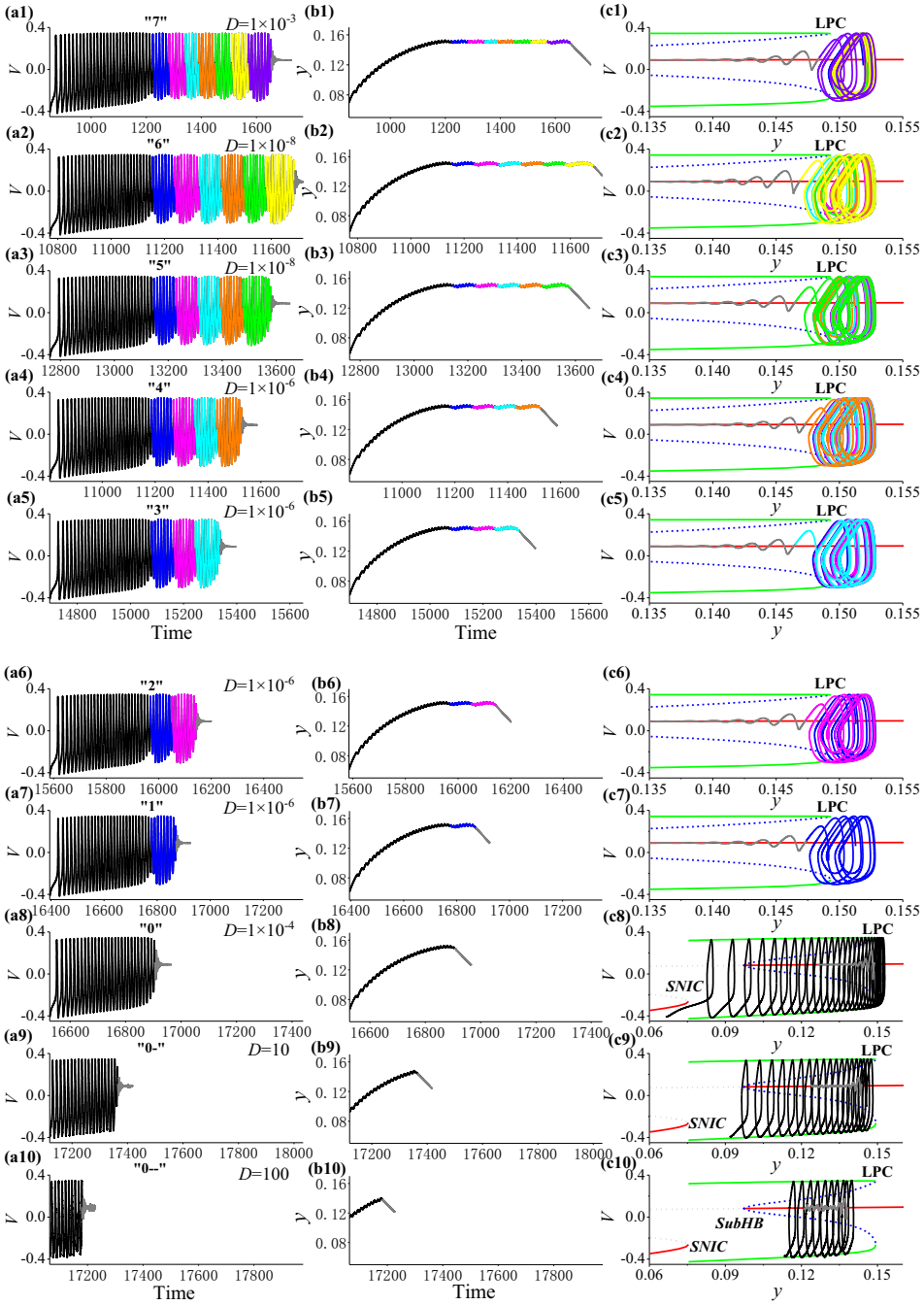


Fig. 8. The V (left), y (middle), and fast–slow dynamics (right) of the stochastic bursts. (a1), (b1), and (c1) '7' for $D = 1 \times 10^{-3}$; (a2), (b2) and (c2) '6' for $D = 1 \times 10^{-8}$; (a3), (b3) and (c3) '5' for $D = 1 \times 10^{-8}$; (a4), (b4) and (c4) '4' for $D = 1 \times 10^{-6}$; (a5), (b5) and (c5) '3' for $D = 1 \times 10^{-6}$; (a6), (b6) and (c6) '2' for $D = 1 \times 10^{-6}$; (a7), (b7) and (c7) '1' for $D = 1 \times 10^{-6}$; (a8), (b8) and (c8) '0' for $D = 1 \times 10^{-4}$; (a9), (b9) and (c9) '0-' for $D = 10$; (a10), (b10) and (c10) '0- -' for $D = 100$.

The fast–slow dynamics of the clusters and SO1 for the first seven examples are shown in the right-hand column, running around the LPC. The number of clusters is influenced by noise. Before moving to be within the ULC, the clusters shuttle back and forth across the LPC several times. For the eighth example (burst '0'), the cluster disappears. After shuttling across the LPC, the behavior changes so that it moves within the ULC, behaving like SO1. Around the LPC, the behavior following subsegment '0' shrinks to the stable focus via SO1. Subsequently, the different bursts and D influence the IBIs and BDs.

3.4.2. Burst at strong D: shortened burst since it terminates in advance

As D becomes large, e.g., $D = 10$, the burst becomes shorter than the basic subsegment '0', labeled as '0-' in Fig. 8(a9). As D further increases to 100, the burst becomes even shorter, labeled as '0- -' in Fig. 8(a10). The strong noise causes the BD to shorten. The fast–slow dynamics are depicted in the right-hand column. The burst terminates at a phase to the left of the LPC, i.e., it terminates earlier, showing that strong noise can have an effect in the region to the left of the LPC. To the left of the LPC, although the stable

branch and the ULC are relatively far from each other, strong noise can cause spiking that changes into subthreshold oscillations, thereby terminating the spike via passage through the ULC. The stronger D is, the further to the left the onset phase of the subthreshold oscillations is, as shown in Figs. 8(c9) and 8(c10). Thus, the different bursts and different levels of D influence the IBIs and BDs.

3.4.3. Initial phase of the burst changes from an SNIC to a region to the right of the SNIC with increasing D

The fast–slow dynamics of SO2, the QS, and the initial phase of the burst are shown in Fig. 9 for different values of D. Deterministic bursting for $D = 0$ is illustrated in Fig. 9(a), and stochastic bursting for $D = 1 \times 10^{-7}$ is shown in Fig. 9(c). As D increases from 1×10^{-7}, SO2 terminates earlier, since the enhanced noise intensity can induce subthreshold oscillations at an earlier stage, as shown in Figs. 9(b)–9(l). The advanced phase induces the longest ISI (the durations of SO1, DB, and SO2 are shortened), which is consistent with our predictions.

For $D < 0.1$, the onset phase of the QS is still to the left of the SNIC, as depicted in Figs. 9(b)–9(h). The phase trajectory still oscillates around the stable node, resulting in a shortened QS. The burst still begins from the SNIC, as shown by the triangles, indicating that the initial phase of the burst is not influenced. The BDs are mainly influenced by the number of clusters. For $D > 0.1$, the phase changes so that it is to the right of the SNIC, as shown in Figs. 9(j)–9(l). Then, the QS disappears, and the burst begins from a region to the right of the SNIC, as shown by the triangles, which shortens the BD. When $D = 100$, the phase is to the right of the subHB. The larger the noise intensity is, the further to the right the phase is. Thus, for large noise intensity, the delayed initial phase of the burst also shortens the BD, not only the righthand end of the burst shown in Fig. 8 ('0-' and '0- -' bursts).

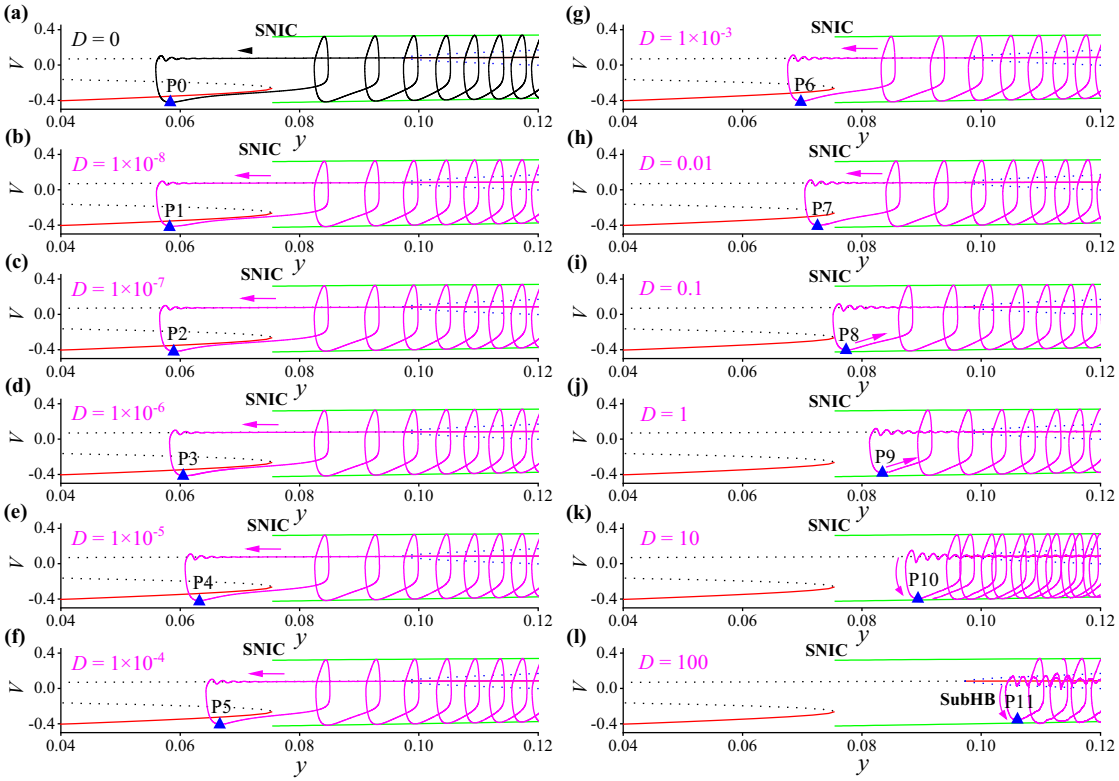


Fig. 9. Fast–slow dynamics of SO2, the QS, and the initial phase of burst at different noise intensities: (a) $D = 0$; (b) $D = 1 \times 10^{-8}$; (c) $D = 1 \times 10^{-7}$; (d) $D = 1 \times 10^{-6}$; (e) $D = 1 \times 10^{-5}$; (f) $D = 1 \times 10^{-4}$; (g) $D = 1 \times 10^{-3}$; (h) $D = 0.01$; (i) $D = 0.1$; (j) $D = 1$; (k) $D = 10$; (l) $D = 100$.

In summary, as illustrated in Figs. 8 and 9, the upper and lower amplitudes of action potentials in mixed-mode bursting generated in stochastic systems are still determined by the stable limit cycle within the bifurcation structure of the fast subsystem. In contrast to deterministic bursting, the onset and termination of the active phase are influenced by noise, altering the positions at which the trajectory leaves the basin of attraction of the limit cycle. Therefore, in the subsequent numerical simulation of the CV, the threshold for action potential firing, which was set to $V = 0.25$ in Subsection 3.1.1, remains valid.

3.5. Transitions between CR and anti-CR

3.5.1. Stochastic bursting trains at different values of D

Stochastic bursting trains for a duration of 10000 at different values of D are depicted in Fig. 10, with D labeled in each panel. Different bursts with different numbers of clusters can appear at a single value of D, while the distribution of the number varies at different values of D. The numbers of bursts exhibit different trends over five ranges of D, which are discussed below.

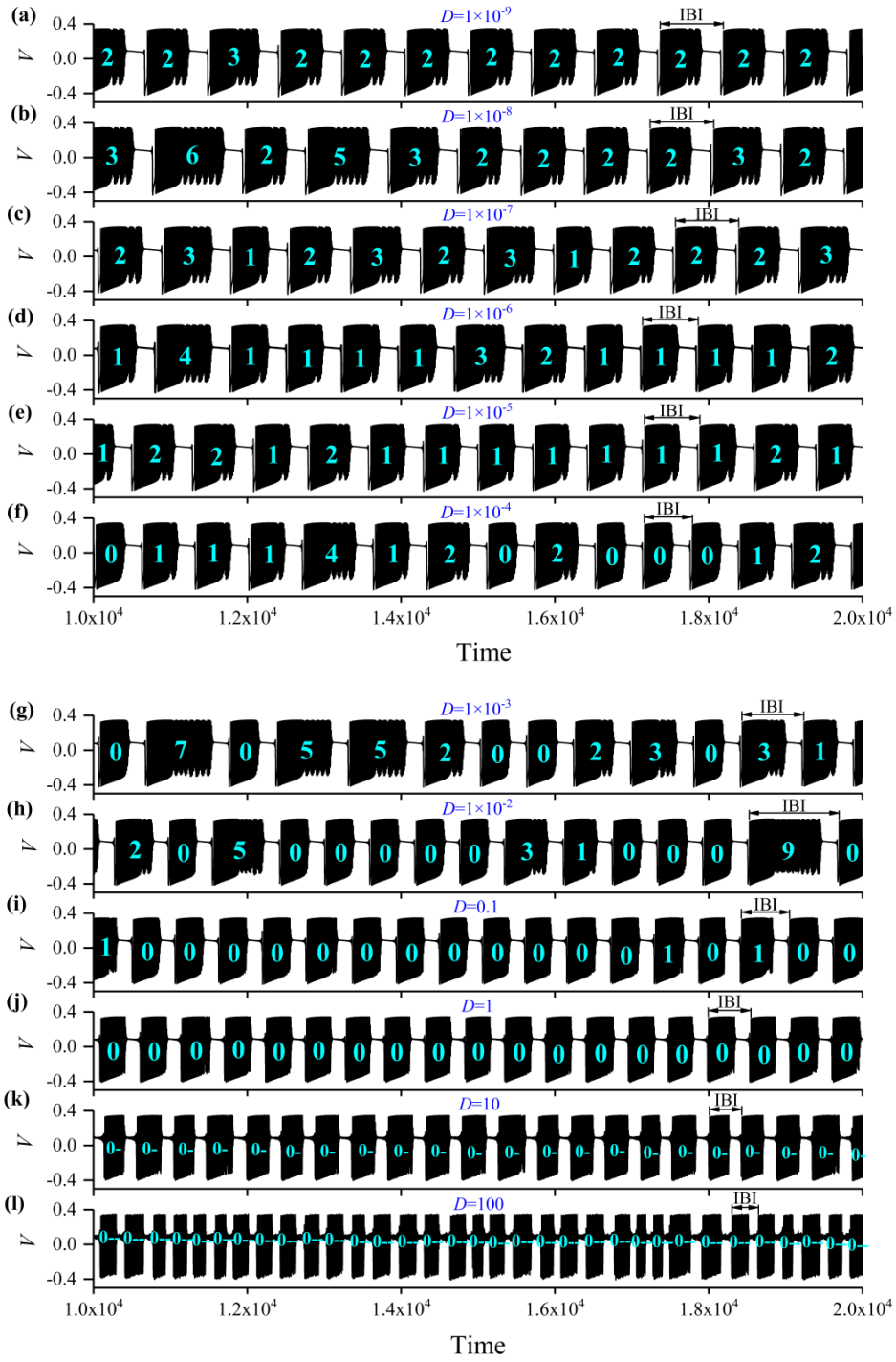


Fig. 10. Stochastic bursting trains at different D: (a) 1×10^{-9}; (b) 1×10^{-8}; (c) 1×10^{-7}; (d) 1×10^{-6}; (e) 1×10^{-5}; (f) 1×10^{-4}; (g) 1×10^{-3}; (h) 1×10^{-2}; (i) 0.1; (j) 1; (k) 10; (l) 100.

The first range is for $D \leq 10^{-7}$ (see Figs. 10(a)–10(c)). As D increases from 10^{-9} to 10^{-8}, bursts of more than two clusters appear and the frequency of appearance of bursts with more than two clusters becomes higher. Thus, it can be predicted that small CVs should appear for BDs and IBIs. For instance, the frequency of bursts with three clusters is 1/12 for $D = 10^{-9}$, and the frequencies of bursts with six, five, and three clusters become 4/12 for $D = 10^{-8}$. As D increases to 10^{-7}, in addition to the bursts with three clusters at a frequency of 4/12, a burst of one cluster appears with a frequency of 2/12, i.e., a shorter burst appears. The burst of two clusters has a frequency of only 6/12. At this point, CVs for BDs and IBIs are still large. This behavior may correspond to anti-CR.

The second range is for $10^{-7} \leq D \leq 10^{-5}$ (see Figs. 10(c)–10(e)). As D increases to 10^{-6}, bursts with one cluster are dominant, occupying 9/13. The frequencies of bursts with four, three, and two clusters are only 4/13. At this point, it can be predicted that the CVs for BDs and IBIs should decrease. For $D = 10^{-5}$, bursts with one cluster still have a frequency of 9/13. However, the bursts of four clusters and three

clusters become fewer. At this point, the CVs for BDs and IBIs are still small. This behavior may correspond to CR.

The third range is for $10^{-5} \leq D \leq 10^{-3}$ (see Figs. 10(e)–10(g)). As D increases to 10^{-4}, four types of bursts appear. The emergence of bursts with cluster size '0' confirms short bursts, occupying 5/14; bursts with one cluster also have a frequency of 5/14, as do those with two and four clusters. The range of cluster numbers widens (zero to four). At this point, it can be predicted that the CVs for BDs and IBIs should increase. For $D = 10^{-3}$, the range of numbers becomes wider (from zero to seven). At this point, the CVs for BDs and IBIs become higher. This behavior may correspond to anti-CR.

The fourth range is for $10^{-3} \leq D \leq 10^{0}$ (see Figs. 10(g)–10(j)). As D increases from 10^{-3} to 10^{0}, the range of numbers becomes smaller and smaller. For $D = 10^{0}$, nearly all bursts become '0', and different individual bursts exhibit small variations, as shown in Fig. 10(j). Then, a small CV appears, showing that CR may appear at $D = 10^{0}$.

The last range is for $D \geq 10^{0}$ (see Figs. 10(j)–10(l)). As D increases to ten, the bursts become shorter, i.e., '0-'. The individual bursts exhibit relatively large variations. At this point, the CV increases. As D increases to 10^{2}, the bursts become even shorter, i.e., '0--'. The individual bursts exhibit large variations. At this point, the CV increases further.

In the stochastic system, it is noteworthy that increasing D shortens the BD and the DB. In numerical simulations, a time interval of 20 is similarly used as the threshold: an ISI exceeding 20 is identified as bursting; otherwise, it is regarded as spiking.

3.5.2. CV of BDs shows multiple transitions between CR and anti-CR

The mean value and SD for the BDs and the corresponding CV are calculated, as illustrated in Figs. 11(a1) and 11(a2). With increasing D, the changes in the SD (red) manifest themselves in five ranges: an increase for $1 \times 10^{-9} < D < 1 \times 10^{-7}$, a decrease for $1 \times 10^{-7} < D < \times 10^{-5}$, an increase for $1 \times 10^{-5} < D < 1 \times 10^{-3}$, a decrease for $1 \times 10^{-3} < D < 1$, and an increase for $1 < D < 100$, as shown in Fig. 11(a1). The mean (blue) exhibits four ranges: an increase for $1 \times 10^{-9} < D < 1 \times 10^{-8}$, a decrease for $1 \times 10^{-8} < D < \times 10^{-5}$, an increase for $1 \times 10^{-5} < D < 1 \times 10^{-4}$, and a decrease for $1 \times 10^{-4} < D < 100$, as shown in Fig. 11(a1). Then, the CV exhibits changes in five ranges, similar to the SD, and the changing trends resemble those of the SD, as depicted in Fig. 11(a2), showing that the SD plays a dominant role. Thus, with increasing D, anti-CR changes to CR, to anti-CR, and then to CR, showing multiple transitions between CR and anti-CR.

3.5.3. CV of IBIs shows multiple transitions between CR and anti-CR

The mean and SD for the IBIs and the corresponding CV are illustrated in Figs. 11(b1) and 11(b2), respectively. As D increases, the changes in the SD (red), mean (blue), and CV resemble those of the BDs. Thus, with increasing D, multiple transitions between CR and anti-CR appear.

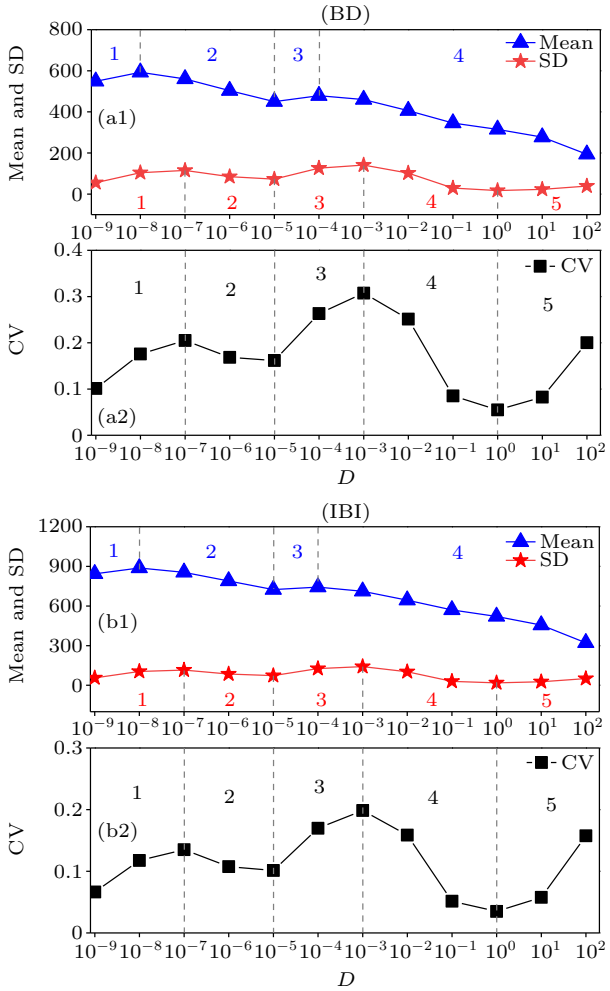


Fig. 11. Transitions between anti-CR and CR: (a1) the mean and SD of the BDs; (a2) the CV for the BDs; (b1) the mean and SD of the IBIs; (b2) the CV for the IBIs.

3.5.4. Spectral analysis shows the same multiple transitions between CR and anti-CR

The average power of $V(t)$ for stochastic bursting at different values of D is presented in Fig. 12(a), and the inset is a magnified view around the low frequencies (< 5 Hz). As D increases from 10^{-9} (green), to 10^{-7} (purple), to 10^{-5} (gray), and to 10^{-3} (dark green), the peak power decreases, increases, and decreases, showing multiple transitions between anti-CR and CR. The peaks appear within 1–2 Hz, corresponding to the IBI for burst '2', which is located around 1.2 Hz. The results are consistent with Fig. 10; the frequency of burst '2' decreases, increases, and decreases from $D = 10^{-9}$, to 10^{-7}, to 10^{-5}, and to 10^{-3}. For $D = 1$, the peak increases, since burst '0' appears and exhibits small variations. The IBI for burst '0' decreases; then, the frequency of the peak becomes high, nearly 2 Hz. For $D = 100$, the peak decreases, since burst '0--' exhibits large variations. The IBI for burst '0--' further decreases; then, the frequency of the peak becomes higher than

3 Hz. The results still show multiple transitions between anti-CR and CR. The changes in peak power with increasing D decrease, increase, decrease, increase, and decrease, as shown in Fig. 12(b), exhibiting changes similar to those of the CV.

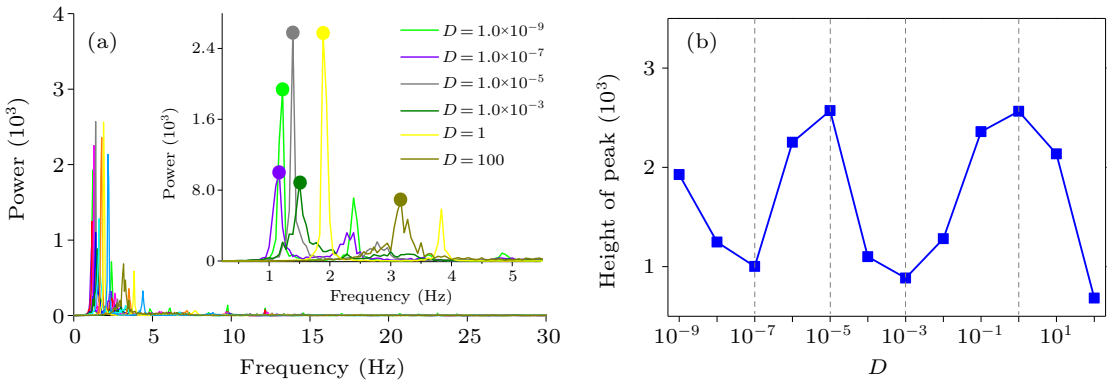


Fig. 12. Average power spectra of stochastic bursting trains: (a) the average power spectrum at different levels of $D = 1\times10^{-9}$ (green), 1×10^{-7} (purple), 1×10^{-6} (magenta), 1×10^{-5} (gray), 1×10^{-4} (blue), 1×10^{-3} (dark green), 1 (yellow), 10 (light blue), 100 (brown). Inset: enlargement of the region around the peak; (b) variation in the height of peak with increasing D.

4. Discussion and conclusion

Our study of CR indicates the positive roles of noise and bursting. The latter, which behaves as a complex rhythm, is a very important nonlinear phenomenon involved in multiple functions in the nervous system. The two phenomena have generally been studied independently in previous studies. In some recent studies, relationships have been established between CR and bursting, which presents novel ways to study the effect of noise in complex neural rhythms.[51–53] In this paper, a novel candidate for CRs in complex bursting is presented, which is significant in the following respects.

On the one hand, mixed-mode bursting exhibits novel dynamics around the termination phase, i.e., the LPC bifurcation, which is more complex than other similar bursting patterns. In general, the burst always terminates directly after passing the bifurcation point for the termination phase. For example, for a subHopf/LPC burst, the burst terminates after the LPC bifurcation point by rapidly shrinking to the stable focus.[50] This view is easily and widely accepted. However, for the SNIC/LPC bursting discussed in this paper, the burst can shuttle back and forth across the LPC twice. This novel result is induced by three factors. The first is the small real part of the eigenvalue of the stable focus. If the real part is more negative, the behavior is attracted to the stable focus, resulting in a drastic shrinking to within the ULC. Then, it moves to the left of the LPC and toward the stable focus to terminate the burst, as in the bursting described in a previous study.[50] Because it does not shrink to the stable focus rapidly, the behavior does not exhibit a small amplitude. The second factor is the y-nullcline modulated by V. The last factor is the coexistence of the stable focus and the SLC, which are separated by the ULC that appears to the left of the LPC. Combined with these factors, the cause for the double passage through the LPC is obtained. Following the last spike of cluster 'II', the amplitude becomes small enough to be inside the ULC and terminate the burst. Two clusters present a novel view of bursting that terminates at the LPC bifurcation.

On the other hand, the multiple transitions between CR and anti-CR are a novel example of CRs for bursting, presenting multiple opportunities to modulate the stochastic responses of bursting, and the underlying bifurcation mechanism is also obtained. In previous studies, single CR, multiple CRs, and anti-CR have been simulated for different bursting patterns.[50–52] Furthermore, the bifurcations for different CRs are obtained with fast–slow dynamics. For example, single CR, multiple CRs, and anti-CR are related to the homoclinic, big homoclinic, and LPC bifurcations. In this paper, transitions from anti-CR, to CR, to anti-CR, and then to CR are simulated, which are more complex than the previous examples. Furthermore, the bifurcation mechanism for the multiple transitions is obtained. For weak noise intensity, noise mainly induces dynamics around the LPC, resulting in different clusters within the burst and various IBIs and BDs. For strong noise intensity, noise mainly induces the behaviors to be delayed relative to the SNIC at the start of the burst and advanced relative to the LPC at the end of the burst, resulting in shortened IBIs and BDs. With increasing noise intensity, the changes in IBIs and BDs induce changes in the CV for the multiple transitions between anti-CR and CR. The changes in the onset and termination phases of the burst for strong noise can easily be understood, similar to those in the previous study.[49] However, the mechanism for weak noise intensity is different from that of the previous study,[50] wherein no clusters appear due to the rapid shrinking of the amplitude around the LPC. In this paper, a slow shrinking of amplitude appears. Multi-CR transition may serve as a coding mode-switching mechanism in neurons: under physiological conditions, it optimizes information transmission in response to noise; under pathological conditions, it is forcibly triggered by abnormal activity, promoting neuronal synchronization and disease propagation.

Previous studies have shown that different neuron models may also produce different types of resonance transitions when stimulated by noise.[50,52] Due to differences in the bifurcation structures among neuron models, there is no unified standard for the forms of these transitions. Although this study has preliminarily explored the transition between CR and anti-CR, a universal criterion applicable across different systems has yet to be established. Future research needs to shift from static description to the analysis of dynamic critical mechanisms, focusing on identifying the key parameters that trigger state transitions. This can be pursued through the following approaches: establishing a critical early warning system that integrates theoretical and data-driven methods to locate critical thresholds; investigating the regulatory mechanisms of noise in state switching; and developing cross-system analogical research to extract universal dynamical criteria. Ultimately, through the integration of multiple methods, it is expected that the transition criteria for CR and anti-CR can be generalized for specific types of complex systems, deepening our understanding of the dialectical relationship between order and disorder in such systems.

Up to now, the stochastic dynamics of bursting patterns have remained open problems. In the future, the stochastic dynamics of various complex bursting patterns and the corresponding bifurcation mechanisms should be studied. For instance, mixed-mode bursting for seizures and migraines has been described using a high-dimensional theoretical model with many modulation parameters and multiple slow variables, with its fast–slow dynamics remaining unclear.[33] The bursting described here resembles bursting associated with seizures and migraines in appearance to a certain extent, so the results of this article may help researchers understand the stochastic bursting associated with seizures and migraines. In addition, complex bursting with physiological significance should be studied in the future.

Appendix A

For the MLT model defined by Eqs. (1)–(3), we perform a coordinate transformation by letting $z = y + I_{\rm app}$. The dynamical equations of the transformed system are then as follows:

$$C\frac{\mathrm{d}V}{\mathrm{d}t} = I_{\rm K} + I_{\rm Ca} + I_{\rm L} + z, \tag{A1}$$

$$\frac{\mathrm{d}\omega}{\mathrm{d}t} = \frac{\omega_\infty - \omega}{\tau_\omega}, \tag{A2}$$

$$\frac{\mathrm{d}z}{\mathrm{d}t} = r(k - V). \tag{A3}$$

After the coordinate transformation, the system equations no longer explicitly contain the parameter $I_{\rm app}$, while all other terms in the equations remain unchanged. Specifically, the presence of $I_{\rm app}$ only induces a rigid translation of the MLT model along the y-axis in phase space, without altering the bifurcation dynamics of the system with respect to the other parameters.

This feature of the MLT model is attributed to the uniqueness of its configuration, wherein $I_{\rm app}$ does not alter the bifurcation structure of the system unless $\mathrm{d}z(y, I_{\rm app})/\mathrm{d}t = \mathrm{d}y/\mathrm{d}t$ is met.

Acknowledgment

Project supported by the National Natural Science Foundation of China (Grant Nos. 12372063 and 12072236).

References

[1] Pikovsky A S and Kurths J 1997 *Phys. Rev. Lett.* **78** 775
[2] Longtin A 1997 *Phys. Rev. E* **55** 868
[3] Gu H G, Yang M H, Li L, Liu Z Q and Ren W 2002 *NeuroReport* **13** 1657
[4] Lindner B, García-Ojalvo J, Neiman A and Schimansky-Geier L 2004 *Phys. Rep.* **392** 321
[5] Izhikevich E M 2000 *Int. J. Bifurcation Chaos* **10** 1171
[6] Lisman J E 1997 *Trends Neurosci.* **20** 38
[7] Izhikevich E M 2007 *Dynamical Systems in Neuroscience* (London: MIT Press)
[8] Jia B and Gu H G 2017 *Int. J. Bifurcation Chaos* **27** 1750113
[9] Wang Y, Ma J, Xu Y, Wu F Q and Zhou P 2017 *Int. J. Bifurcat. Chaos* **27** 1750030
[10] Chen Y X, Guo Y T, Wang C N and Zhu Z G 2025 *Chaos Solit. Fract.* **199** 116799
[11] Guo Q, Zhou P, Zhang X F and Zhu Z G 2025 *Cogn. Neurodyn.* **19** 75
[12] Chen Y X, Yang F F and Wang C N 2024 *Mod. Phys. Lett. B* **39** 2550008
[13] Li Y N, Guo Q, Wang C N and Ma J 2024 *Commun. Nonlinear Sci. Numer. Simul.* **139** 108320
[14] Bashkirtseva I and Ryashko L 2023 *Chaos Solit. Fract.* **170** 113414
[15] Lacasta A M, Sagués F and Sancho J M 2002 *Phys. Rev. E* **66** 045105
[16] Lu L L, Jia Y, Ge M Y, Xu Y and Li A B 2020 *Nonlinear Dyn.* **100** 877
[17] Yilmaz E, Ozer M, Baysal V and Perc M 2016 *Sci. Rep.* **6** 30914
[18] Perc M 2005 *Phys. Rev. E* **72** 016207
[19] Sun X J, Perc M, Lu Q S and Kurths J 2008 *Chaos* **18** 023102
[20] Gu H G, Jia B, Li Y Y and Chen G R 2013 *Physica A* **392** 1361
[21] Warden M C A, McAllister J C, Cruse D, Wright B and MacDonald H J 2025 *NPJ Parkinsons Dis.* **11** 12345
[22] Tang X, Jaenisch R and Sur M 2021 *Nat. Rev. Neurosci.* **22** 290
[23] Hesse J, Schleimer J H, Maier N, Schmitz D and Schreiber S 2022 *Nat. Commun.* **13** 3934
[24] Arinyo-I-Prats A, Moreno-Spiegelberg P, Matias M A and Gomila D 2021 *Phys. Rev. E* **104** L052203
[25] Gu J H, Laszik N, Miles E C, Allard J, Downing L T and Read L E 2025 *Bioinformatics* **41** btaf581
[26] Zhang K N, Zhao Y C, Hu Q X, Zhang H Y, Choi S H, Chen G B and Lan Y 2026 *J. Clin. Neurosci.* **144** 111793
[27] Li R Z, Yang S, Feng K K, Yao Y, Wang L L, Yin S Y and Xu G Z 2026 *Next Res.* **4** 101220
[28] Abobda T L 2025 *Sci. Rep.* **15** 33859
[29] Saji J, Dainotti G M, Bhardwaj S and Janiuk A 2025 *Astron. Astrophys.* **702** A13
[30] Fan D G, Zheng Y H, Yang Z C and Wang Q Y 2020 *Appl. Math. Mech. Engl. Ed.* **41** 1287
[31] Yang Y, Cui Y H, Sang K N, Dong Y Y, Ni Z Y, Ma S S and Hu H L 2018 *Nature* **554** 317
[32] Ma K H, Gu H G and Jia Y B 2024 *Cogn. Neurodyn.* **18** 1397
[33] Wei Y N, Ullah G and Schiff S J 2014 *J. Neurosci.* **34** 11733
[34] Li Y Y, Gu H G and Qi C S 2025 *Cogn. Neurodyn.* **19** 59
[35] Warden A C M, McAllister C J, Cruse D and MacDonald H J 2025 *Park. Relat. Disord.* **134** 107582
[36] Ali G 2022 *Int. J. Mol. Sci.* **23** 5744

[37] Norby J H, Hummel D, Ricks N, Rolston J, Rahimpour S, Cowan R, Voiplo J, Trevelyan A J, Smith E H and Parrish R R 2025 *Neurobiol. Dis.* **211** 106937

[38] Stojanovic S, Knowlton C J, Mackrodt R E, Mankel J, Shin J, Lammel S, Canavier C C and Roeper J 2025 *J. Neurosci.* **45** e0361252025

[39] Elliott M A T, Andrews J P, Molen T V D, Geng J, Spaeth A, Toledo A, Voltiuk K, Core C, Gillespie T, Sinervo A, Parks D F, Robbins A, Solis D, Chang E F, Nowakowski T J, Teodorescu M, Haussler D and Sharf T 2026 *J. Neurophysiol.* **135** 273

[40] Rinzel J 1987 *A formal classification of bursting mechanisms in excitable systems* (Berlin: Springer-Verlag)

[41] Yang Z Q, Lu Q S and Li L 2006 *Chaos Solit. Fractals* **27** 87

[42] Wen Q X, Liu S Q and Lu B 2021 *Electron. Res. Arch.* **29** 3205

[43] Han X J, Bi Q S, Zhang C and Yu Y 2014 *Int. J. Bifurcation Chaos* **24** 1450098

[44] Duan L X, Liu J, Chen X, Xiao P C and Zhao Y 2017 *Cogn. Neurodyn.* **11** 91

[45] Zhang X Y, Li M L, Xu X and Bi Q S 2026 *Int. J. Bifurcation Chaos* **36** 2650048

[46] Shao Y, Wu F Q and Wang Q Y 2025 *Nonlinear Dyn.* **113** 33907

[47] Hua H T, Gu H G, Jia Y B and Li Y Y 2025 *Nonlinear Dyn.* **113** 25153

[48] Faisal A A, Selen L P J and Wolpert D M 2008 *Nat. Rev. Neurosci.* **9** 292

[49] McDonnell M D and Ward L M 2011 *Nat. Rev. Neurosci.* **12** 415

[50] Guan L N, Gu H G and Jia Y B 2020 *Nonlinear Dyn.* **100** 3645

[51] Cao B, Wang R X, Gu H G and Li Y Y 2021 *Cogn. Neurodyn.* **15** 77

[52] Hua H T, Gu H G, Jia Y B and Lu B 2022 *Commun. Nonlinear Sci. Numer. Simul.* **110** 106370

[53] Cao B, Gu H G and Zhao Z G 2025 *Chaos Solit. Fractals* **200** 116963

[54] Lv G Y, Xu T Y, Chen F Y, Zhu P, Wang M and He G G 2024 *Chin. Phys. B* **33** 028704

[55] Zhang Y Q and Lei Y M 2024 *Chin. Phys. B* **33** 038201

[56] Slepukhina E, Kügler P, Bashkirtseva I and Ryashko L 2023 *Int. J. Bifurcation Chaos* **33** 2350159

[57] Terman D 1991 *SIAM J. Appl. Math.* **51** 1418

[58] Ermentrout B 2002 *Simulating, Analyzing, and Animating Dynamical Systems: A Guide to XPPAUT for Researchers and Students* (Philadelphia: SIAM)